Structural and antibacterial studies of novel ZnO and $Zn_xMn_{1-x}O$ nanostructured titanium scaffolds for biomedical applications

Giovanna Calabrese[1‡], Giovanna De Luca[1‡], Domenico Franco[1], Dario Morganti[2], Maria Giovanna Rizzo[1], Anna Bonavita[3], Giovanni Neri[3], Enza Fazio[4], Fortunato Neri[4], Barbara Fazio[5], Francesco Crea[1], Antonio Alessio Leonardi[6], Maria Josè Lo Faro[6], Salvatore Guglielmino[1] and Sabrina Conoci[1,5,7,8]*

[1]Department of Chemical, Biological, Pharmaceutical and Environmental Sciences (ChiBioFarAm), University of Messina, Viale F. Stagno d'Alcontres 31, 98166 Messina, Italy

[2]IBMTECH s.r.l, Via Napoli 116, Catania (Italy).

[3]Department of Engineering, University of Messina, Viale F. Stagno d'Alcontres 31, 98166 Messina, Italy

[4]Department of Mathematical and Computational Sciences, Physics Science and Earth Science, University of Messina, Viale F. Stagno D'Alcontres 31, 98166 Messina, Italy

[5]LAB Sense Beyond Nano - URT Department of Sciences Physics and Technologies of Matter (DSFTM) CNR, Viale F. Stagno d'Alcontres 31, 98166 Messina, Italy;

[6]Department of Physic and Astronomy, University of Catania (Italy), Via Santa Sofia 64, Catania, Italy

[7]Istituto per la Microelettronica e Microsistemi, Consiglio Nazionale delle Ricerche (CNR-IMM) Catania, Italy

[8]Department of Chemistry ‘‘Giacomo Ciamician’’, University of Bologna, Via Selmi 2, 40126 Bologna, Italy

‡These authors contributed equally to this work.

KEYWORDS:

ZnO, $Zn_xMn_{1-x}O$, nanomaterials, antibacterial activity, implantable-device, titanium scaffolds

HIGHLIGHTS:

- First study in the literature describing ZnO and Mn-doped ZnO NPs nanofunctionalized Ti scaffolds with improved antibacterial performance.
- Complete eradication for S. aureus
- 90% of reduction for P. aeruginosa
- Antibacterial mechanism investigated and attributed to both Zn2+ and Mn2+ metal ions release
- Coating strategy suitable for realization of new hybrid implantable devices through a low-cost process, compatible with the biotechnological industrial chain method.

ABSTRACT

In the biomedical field, the demand for the development of broad-spectrum biomaterials able to inhibit bacterial growth is constantly increasing. Chronic infections represent the most serious and devastating complication related to the use of biomaterials. This is particularly relevant in the orthopaedic field, where infections can lead to implant loosening, arthrodesis, amputations and sometimes death. Antibiotics are the conventional approach for implanted-associated infections, but they have the limitation of increasing antibiotic resistance, a critical worldwide healthcare issue. In this context, the development of anti-infective biomaterials and infection-resistant surfaces can be considered the more effective strategy to prevent the implant colonisation and biofilm formation by bacteria, so reducing the occurrence of implant-associated infections. In the last years, inorganic nanostructures have become extremely appealing for chemical modifications or coatings of Ti surfaces, since they do not generate antibiotic resistance issues and are featured by superior stability, durability, and full compatibility with the sterilization process. In this work, we present a simple, rapid, and cheap chemical nanofunctionalization of titanium (Ti) scaffolds with colloidal ZnO and Mn-doped ZnO nanoparticles (NPs), prepared by a sol-gel method, exhibiting antibacterial activity. ZnO NPs and $Zn_xMn_{(1-x)}O$ NPs formation with a size around 10–20 nm and band gap values of 3.42 eV and 3.38 eV, respectively, have been displayed by characterization studies. UV–Vis, fluorescence, and Raman investigation suggested that Mn ions acting as dopants in the ZnO lattice. Ti scaffolds have been functionalized through dip coating, obtaining ZnO@Ti and $Zn_xMn_{(1-x)}O$@Ti biomaterials characterized by a continuous nanostructured film. ZnO@Ti and $Zn_xMn_{(1-x)}O$@Ti displayed an enhanced antibacterial activity against both Gram-positive *Staphylococcus aureus* (*S. aureus*) and Gram-negative *Pseudomonas aeruginosa* (*P. aeruginosa*) bacterial strains, compared to NPs in solution with better performance

of $Zn_xMn_{(1-x)}O$@Ti respect to ZnO@Ti. Notably, it has been observed that $Zn_xMn_{(1-x)}O$@Ti scaffolds reach a complete eradication for *S. aureus* and 90 % of reduction for *P. aeruginosa*. This can be attributed to Zn^{2+} and Mn^{2+} metal ions release (as observed by ICP MS experiments) that is also maintained over time (72 h). To the best of our knowledge, this is the first study reported in the literature describing ZnO and Mn-doped ZnO NPs nanofunctionalized Ti scaffolds with improved antibacterial performance, paving the way for the realization of new hybrid implantable devices through a low-cost process, compatible with the biotechnological industrial chain method.

1. Introduction

In the biomedical field, there is an increasing demand to develop broad spectrum biomedical devices able to inhibit bacterial growth [1,2]. Microbial infections are one of the most important causes leading to mortality and morbidity among surgical patients [[3], [4], [5]].

The infection risk is considered as the most serious and devastating complication related to the use of biomaterials, in many medical fields. This is particularly relevant in the orthopaedic field, where infections can eventually evolve into osteomyelitis, which is responsible for severe effects on both bone and surrounding soft tissues [[6], [7], [8]]. Further, chronic infections that not response to the conventional antibiotic therapy can lead to implant loosening, arthrodesis, amputations and sometimes death [9].

Titanium (Ti) alloys are the most used material for permanent artificial implants due to their excellent mechanical and chemical properties [[10], [11], [12]], corrosion resistance [13,14] and biocompatibility [15,16]. Unfortunately, these materials can also provide a good foothold for pathogenic bacteria that colonise them, forming biofilms hard to eradicate [17,18]. *S.*

aureus (Gram-positive) is the most frequent cause of orthopaedic implant infections [19] featured by several virulence factors, such as coagulase and adhesion proteins that induce the escape from the host immune system, leading to bacterial invasion and osteolysis of the tissue around implants [20]. Gram-negative bacteria can also be involved in the infections associated with fracture-fixation implantable devices [21]. They generally include species belonging to Enterobacteriaceae and other bacilli, such as *P. aeruginosa*, able to produce a biofilm hard to eradicate, associated with poor healing in fracture-related infections [22].

Antibiotics are the conventional approaches to avoid implant-associated infection [23,24]. However, these treatments have the limitation of increasing antibiotic resistance by microbial strains, which is a critical worldwide healthcare issue [25]. Additionally, antibiotics do not eliminate infection risks that can be furtherly caused by some drug-resistant variants (secondary infections) with more acute clinical manifestations [26].

In this context, the development of anti-infective biomaterials and of infection-resistant surfaces can be considered the more effective strategy to prevent the implant colonisation and biofilm formation by bacteria, so reducing the occurrence of implant-associated infections [27]. Several works have reported chemical modifications of the Ti surface or applications of coatings to confer antibacterial properties [[28], [29], [30]]. Most of these chemical modifications involve organic materials that, although show effective antibacterial properties however have the limitation of poor stability and compatibility with industrial sterilization processes. Therefore, inorganic materials with bactericidal activity gained considerable interest, due to their superior stability, durability, and thermal resistance [31,32]. Among these, the most extensively studied material is the silver (Ag) [[33], [34], [35]]. However, Ag is a precious metal that rapidly oxidizes when exposed to light and heat and exhibits a cytotoxic effect [33,36].

Metal and metal oxide nanoparticles represent a promising alternative due to their broad-spectrum antibacterial activity. This involves several mechanisms that are not entirely clarified and still controversial since they include several NPs properties such as the size and their surface features (charge, isoelectric point…). Basically, the main mechanisms that have been reported are: (i) direct contact of NPs with cell walls; (ii) ion leaching/dissolution, and (iii) Reactive Oxygen Species (ROS) production [37].

Among nanomaterials, metal oxide nanostructures, like ZnO NPs [38,39], CuO NPs [40,41], NiO NPs [42], and MnO [5,43] NPs, have been extensively studied as antibacterial agents due to their ease synthesis and versatile properties.

ZnO is the most biosafe semiconductor material with good electrical and optical properties [44]. Nano-sized ZnO (ZnO NPs) display high biocompatibility [45], biodegradability over time, through the excretion of the excess zinc by the body [46], and efficient bactericide properties with the ability to inhibit both Gram-positive and Gram-negative bacteria without inducing antibiotic resistances [[44],[47], [48], [49], [50], [51], [52], [53]]. ZnO NPs are also investigated in various tissue regeneration applications [54,55]. The doping of ZnO with several metals (Cr, Mn, Fe, Co, and Ni) has also been explored [56]. In the literature various methods for the synthesis of pure and doped ZnO NPs through physical, chemical, and biological approaches are reported. Laser ablation [57], arc discharge [58], combustion methods [59], flame spry pyrolysis [60], hydrothermal [61], and Chemical Vapor Deposition (CVD) are the most used techniques. Although all these techniques allow the synthesis of doped NPs below 100 nm, they suffer of several drawbacks. These approaches require high process temperatures, long synthesis times, and specific and expensive equipment that may limit their diffusion as not available to everyone.

Among the several strategies, the wet chemical synthesis in solution has been preferred, being rapid, simple, and low cost with respect the above-mentioned techniques. In literature, $Zn_xMn_{(1-x)}O$ NPs are mainly synthesized by coprecipitation of Zn^{2+} and Mn^{2+} metal ions in different ratios of the starting precursors [62]. In the literature, different metal precursors have been used, the ideal candidate being Zn^{2+} and Mn^{2+} acetates. Even bigger structures such as Mn-doped zinc oxide microspheres are synthesized by coprecipitation of Zn^{2+} and Mn^{2+} ions starting from $Zn(CH_3COO)_2$ and $Mn(CH_3COO)_2$ [63]. The literature reports synthesis of ZnO and $Zn_xMn_{(1-x)}O$ nanoparticles by ions coprecipitation in different solvents [64,65].

Metal-doped ZnO has been shown to improve the antibacterial properties of ZnO due to the introduction of new energy levels that improve the ROS production ability [66,67].

Among transition metals, Mn represents an important micro-nutrient for the metabolism, growth, and reproduction of living organisms [[68], [69], [70]] and is a key element also for connective tissue and bone growth [71]. It gives rise to different metal oxide forms, such as MnO, MnO_2, Mn_2O_3, Mn_3O_4, and Mn_5O_8 (Mn_xO_y) [72]. Mn NPs have also been widely considered and explored, and they showed good antimicrobial properties against both Gram-positive and Gram-negative bacteria [[3], [4], [5]]. Although the antibacterial activity of Mn-doped ZnO NPs against different bacterial strains is well established [[73], [74], [75]], to the best of our knowledge, nanocoating's of these materials on titanium scaffolds are poorly investigated and have not been reported to date.

In this work, we present a simple, rapid and cheap chemical nanofunctionalization of Ti scaffolds with colloidal Mn-doped ZnO NPs obtained via Zn(II) and Mn(II) acetate salts as metal precursors in DMSO solvent, able to stabilize the nanostructures. We investigated the morphological and

structural features of the nano-functionalized Ti scaffolds (ZnO@Ti and $Zn_xMn_{(1-x)}O$@Ti) and their antibacterial properties. Results are presented and discussed.

2. Materials and Methods

Chemicals. Zn(II) acetate dihydrate, Mn(II) acetate tetrahydrate, tetramethylammonium hydroxide (25 wt%), dimethyl sulfoxide (DMSO, HPLC and biological grade), hydrogen peroxide (30 % v/v), ammonium hydroxide (30 % v/v), and ultra-pure water (UPW) were purchased by Sigma-Aldrich. Commercial Si wafers were purchased from Siegert Wafer.

ZnO nanoparticles (NPs) synthesis. ZnO NPs synthesis was carried out according to Panasiuk et al. [76]. An aqueous solution of $N(CH_3)_4OH$ (25 % w/w, 0.3 mL) was rapidly added under vigorous stirring to 19.7 mL of a DMSO solution of Zn^{2+} ions (final $[Zn^{2+}] = 0.2$ M), obtaining a 1:2 ratio between $[M^{2+}]$ and $[OH^-]$. The initially transparent solution immediately turned cloudy white due to the precipitation of ZnO NPs. Then suspensions were kept under stirring for 30 min at room temperature (RT) and purified thrice by centrifugation (5000 rpm, 10 min). The solid was finally resuspended in DMSO (≥99 %), through sonication for 10 min at RT, up to a nominal ZnO NPs amount of 16.3 mg/mL.

$Zn_xMn_{1-x}O$ NPs synthesis. The synthesis of $Zn_xMn_{(1-x)}O$ NPs was carried out according to a slight modification of Panasiuk et al. [76]. An aqueous solution of $N(CH_3)_4OH$ (25 % w/w, 0.3 mL) was added to 19.7 mL of a DMSO solution containing a mixture of Zn^{2+} and Mn^{2+} ions (final $[M^{2+}] = 0.2$ M; $Zn^{2+}/Mn^{2+} = 0.975/0.25$) under vigorous stirring, in a 1:2 ratio between $[M^{2+}]$ and $[OH^-]$. The initially transparent and colourless solution immediately turned cloudy brown due to the precipitation of $Zn_xMn_{(1-x)}O$ NPs. After suspensions were kept under stirring for 30 min at RT

and purified thrice by centrifugation (5000 rpm, 10 min). The solid was finally resuspended in DMSO through sonication for 10 min at RT, up to a nominal $Zn_xMn_{(1-x)}O$ NPs amount of 16.3 mg/mL.

NPs deposition on Ti scaffolds. Trabecular Ti scaffolds (1 cm × 1 cm × 0.26 cm) have been provided by MTOrtho Inc., and they were constituted by Ti-6Al-4V alloy. They were cleaned by immersion in a basic piranha solution, prepared by mixing UPW, 30 wt% H_2O_2, and 30 wt% NH_4OH in a 2:1:1 volume ratio, at 80 °C under magnetic stirring for 20 min. The samples were thoroughly washed with UPW to eliminate any cleaning solution residue. A slight blackening of the Ti substrate metallic gray surface was observed after the cleaning protocol. ZnO or $Zn_xMn_{(1-x)}O$ NPs were then deposited onto Ti scaffolds by dipping (1–2 s) followed by samples drying in an oven at 50 °C for 8 h. Finally, the samples were washed thrice in UPW under gentle oscillation at 37 °C and air-dried.

UV-Vis measurements. UV–vis absorption spectra of NP suspensions (27 μg/mL) were recorded in 1 cm quartz cuvettes on a Jasco V-570 spectrophotometer operating with 2 nm slits. The direct band gap E_g of nanomaterials is derived from the Tauc plot [77] which presents the relationship between the optical absorption coefficient α and the incident photon energy hυ:

$$(\alpha h\upsilon)^2 \sim (h\upsilon - E_g)$$

The E_g value is the intercept between the x-axis and the tangent to the linear section of the band edge.

Photoluminesce measurements. Fluorescence emission spectra of NPs suspensions (27 μg/mL) were recorded in 1 cm quartz cuvettes on a HoribaJobin Yvon FluoroMax-P fluorimeter equipped

with a Hamamatsu R3896 photomultiplier. The spectra were recorded operating in a right-angle geometry, a 333 nm excitation wavelength with 5 nm slits, and a high-pass filter with a cut-off of 400 nm.

Micro-Raman spectroscopy. The samples before to be investigated by Raman spectroscopy were prepared by drop casting 200 μL of 16.3 mg/mL NP suspensions onto 1 cm × 1 cm glass slides and drying samples in an oven at 50 °C for 4 h. Raman spectra were acquired using a Micro-Raman HR800 (Horiba) equipped with a 100× objective (N.A. = 0.9), and the 514.5 nm line of an Ar^{2+} laser with a power density of 2 mW/μm^2 and acquisition time of 60 s. The instrument was equipped with a Peltier-cooled CCD model "Synapse" (Horiba). Grating: 1800 grooves/mm.

Scanning Electron Microscopy (SEM) and Energy Dispersive X-ray (EDX) Analyses. NPs morphology was examined by dip-coating Si wafers chips into their suspensions and drying the samples in air at RT. SEM micrographs were recorded at an acceleration voltage of 5 kV using a Gemini Field Emission SEM (FE-SEM) Zeiss SUPRA 25 equipped with an InLens detector.

The morphology of NPs coated Ti scaffolds was investigated using a Zeiss Crossbeam 540 FE-SEM instrument operating at acceleration voltage in the 3–15 kV range in the analytical and high-resolution modes, equipped with the Oxford Instruments XMax^N 150 EDX probe. EDX data were collected under the same accelerating voltage (10 kV), working distance (5 mm), and image magnification (10,000×).

SEM in the transmission mode (STEM) analyses were carried out with a Zeiss-Gemini 2 electron microscope, operating at 30 kV, with a working distance of 4 mm and at an accelerating voltage of 150 kV.

Measurement of Zn^{2+} and Mn^{2+} metal ion release from Ti scaffolds: The released amount of both Zn^{2+} and Mn^{2+} metal ions from the surface of the ZnO@Ti and $Zn_xMn_{(1-x)}O$@Ti scaffolds was

assessed as follows. Two scaffolds for type were separately incubated in 1 mL of UPW for 24 h under constant stirring. After 24 h, the supernatants were collected, and another 1 mL of UPW was added to each scaffold. This process was repeated until to 72 h. At the end of the procedure, two aliquots for each time (one for each scaffold) were collected and mixed. 1.6 mL of each solution was withdrawn and diluted to a final volume of 3.2 mL. The two solutions of 3.2 mL relating to 24 h and 72 h were analyzed by inductively coupled plasma mass spectrometry, using an Agilent model 7900 instrument equipped with a single quadruple and using the UNI EN ISO 17294-2 method. Certified standard solutions (from AreaChem Instruments and Consumables (Naples, Italy)) of individual metals (1000 mg/L in aqueous solution with 5 % nitric acid) and mix of metals (100 mg/L in aqueous solution with 2 % nitric acid), were used for the analysis. For each metal cation, the calibration curves were constructed in the concentration range between 0.5 and 100 µg/L (ppb), exhibiting a linearity of the instrumental response ($R > 0.9998$). As required by the UNI EN ISO 17294-2 method, a solution containing Sc, Y and Re (500 ppb) was also prepared and analyzed as an internal standard.

Bacterial strains, media, and growth conditions. P. aeruginosa (ATCC27853) and *S. aureus* (ATCC29213) were purchased from the American Type Culture Collection (LGC Promochem, Milan, Italy) and cultured in Luria-Bertani broth (LB, Sigma-Aldrich, Milan) and tryptone soy broth (TSB, Sigma-Aldrich, Milan), respectively. Both bacterial strains were maintained in their respective media supplemented with 20 % glycerol at −80 °C.

Minimal inhibitory concentration (MIC): MIC was determined by broth microdilution assay. For each strain, semi-exponential broth culture was prepared at a final concentration of about 10^5 bacteria/mL starting from 0.5 Mc Farland inoculum (~1.5×10^8 bacteria/mL). Bacterial suspensions, dispensed in tubes, were incubated with several ZnO and $Zn_xMn_{(1-x)}O$ NPs

concentrations (600, 300, 150, 75, and 37.5 μg). Then, 150 μL from each experimental condition were distributed in 96-well plates and incubated at 37 °C for 18 h. Finally, bacterial growth was quantified by spectrophotometric reading at 540 nm (OD_{540}) with a microtiter plate reader (Multiskan GO, Thermo Scientific, Waltham, MA-USA). All samples were analyzed in triplicate. The bactericidal activity was calculated by % OD_{540nm} by using the following formula:

$$\text{Normalized } OD_{540nm} = (OD_{540nm}\ MO - OD_{540nm}\ \text{blank}) / OD_{540nm}\ \text{blank}$$

where MO = ZnO NPs and $Mn_xZn_{(1-x)}O$ NPs.

MIC was evaluated by considering over 90 % of % bacterial inhibition with respect to the control + (bacterial culture without NPs) using the following formula:

% Bacterial inhibition = (% OD_{540nm}CTR+ − %OD_{540nm}MO NPs)/ %OD_{540nm} CTR+

MIC = % bacterial inhibition > 90 %.

Evaluation of antibacterial activity of ZnO and $Zn_xMn_{(1-x)}O$ NPs coated titanium scaffolds (ZnO@Ti and $Zn_xMn_{(1-x)}O$@Ti) on planktonic cells: For each strain, bacterial suspensions were incubated in a 24-well plate with several types of pre-decontaminated titanium scaffolds: uncoated titanium scaffold (Ti) and coated titanium scaffolds with ZnO NPs (ZnO@Ti) and $Zn_xMn_{(1-x)}O$ NPs ($Zn_xMn_{(1-x)}O$@Ti). Then, the plate was incubated under gentle shaking (100 rpm, orbital shaker KS-15, Edmund Bühler GmbH) at 37 °C for 24 h. Cell viability was evaluated by XTT assay and expressed as a percentage of the uncoated Ti. More in detail, 100 μL of bacterial cultures, from each experimental condition, were transferred in a 96-well plate and 25 μL of XTT solution, prepared according to the manufacturing protocol, was added. Then, the plate was incubated for 90 min at 37 °C in the dark. After incubation period, the plate was shaken briefly and OD at 490 nm

(OD_{490}) measured by using a synergy HT plate reader (BioTek Instruments, Inc., VT, United States). All samples were analyzed in triplicate.

Evaluation of antibacterial activity of ZnO and $Zn_xMn_{(1-x)}O$ NPs coated titanium scaffolds (ZnO@Ti and $Zn_xMn_{(1-x)}O$@Ti) on adhered cells: To detect viable and sessile cells after 24 h of incubation, Ti scaffolds were aseptically transferred into 24-well plate and washed gently thrice with phosphate buffer saline (PBS) to remove non-adherent bacteria. Then, each scaffold, placed in a conical tube, was vortexed for 60 s in PBS, and the detached bacteria were quantified through Colony Forming Units (CFU) assay, as previously reported [30]. Precisely, bacterial suspensions were serially diluted in PBS, and finally 100 µL of each dilution were spread on agar plates. Agar plates, then, were incubated overnight at 37 °C and CFU number determined. CFU/mL was quantified by the following formula:

$$\mathrm{CFU/mL} = \frac{\text{number of colonies}}{\text{volume (0.1mL) x dilution factor}}$$

All samples were analyzed in triplicate.

Statistical analysis. Data were analyzed either as raw data or as mean ± standard error (SE), as appropriate. Differences between scaffolds were evaluated by using two-way ANOVA with post-hoc Holm test, where appropriate. The values $p < 0.05$ were considered significant.

3. Results and Discussion

The ZnO@Ti and $Zn_xMn_{(1-x)}O$@Ti scaffolds were prepared according to the scheme reported in Fig. 1. Basically, cleaned trabecular Ti were dipped into solutions containing pre-synthetized ZnO and $Zn_xMn_{(1-x)}O$ NPs. The procedure involves few steps and is quick and easy to perform.

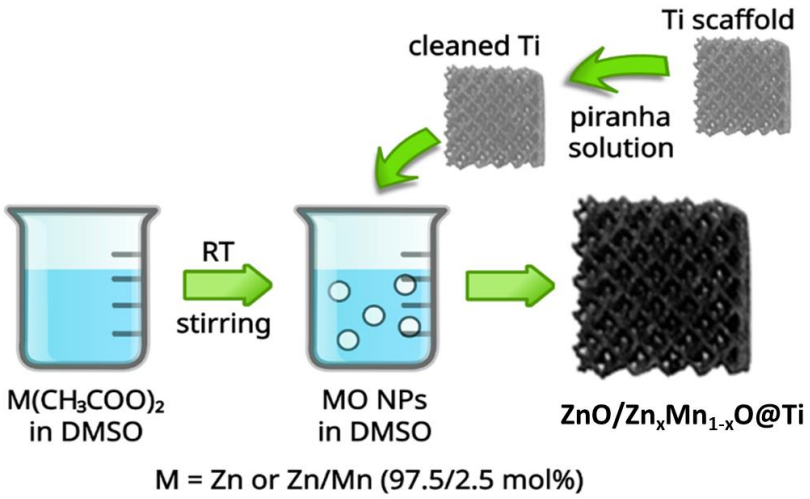

Fig. 1. Schematic representation of the synthesis and deposition process of ZnO and $Zn_xMn_{(1-x)}O$ NPs on Ti scaffold.

ZnO and Mn-doped ZnO NPs syntheses are carried out following the literature method reported in [76], which presents several advantages both from the nano chemical and the biological point of view. This approach can yield a colloid of luminescent semiconductor nanospheres smaller than 10 nm, very stable toward self-aggregation even in relatively high concentrations. DMSO allows the stabilization of the colloid, avoiding the extensive precipitation that can occur in water solutions. Actually, in our study, ZnO and $Zn_xMn_{(1-x)}O$ NPs form via a precipitation reaction upon the addition of tetraethylammonium hydroxide to a Zn^{2+} or a Zn^{2+}/Mn^{2+} (0.975:0.025 mol%) solution in DMSO. According to the literature, avoiding water as a solvent lead to the fast dehydration of the sparingly soluble metal hydroxides and the direct formation of a stable colloid of oxides (Eqs. (1), (2)):

$$Zn^{++} + 2\ OH^{-} \rightleftharpoons Zn(OH)_{2\ (s)} \rightleftharpoons ZnO_{(s)} + H_2O \quad \text{(Eq. 1)}$$

$$x\ Zn^{++} + (1 - x)\ Mn^{++} + 2\ OH^{-} \rightleftharpoons Zn_xMn_{1-x}(OH)_{2\ (s)} \rightleftharpoons Zn_xMn_{1-x}O_{(s)} + H_2O \quad \text{(Eq. 2)}$$

Fig. 2a presents UV–vis absorption and photoluminescence features of the obtained white ZnO and brown $Zn_xMn_{(1-x)}O$ NP suspensions (Fig. 2a, inset: left and right vial, respectively). The absorption spectrum of ZnO (solid black line) displays a continuous band with an edge around 355 nm (3.49 eV) and a peak centred around 337 nm (3.68 eV), together with a broad fluorescence emission (dashed black line) centred around 568 nm (2.18 eV, $\lambda_{exc} = 333$ nm). These results are in agreement with previous studies [[76], [77], [78]] that assigned this fluorescence emission to an electron transition from a level close to the edge of the conduction band to a deeply trapped hole in the bulk of the ZnO particle [79]. The 3.42 eV value for the NPs (direct) band gap, as determined per the Tauc plot [77] (Fig. 2b), is slightly higher than the band gap of bulk ZnO (3.2–3.3 eV) [80], suggesting a quantum confinement of the photogenerated excitons.

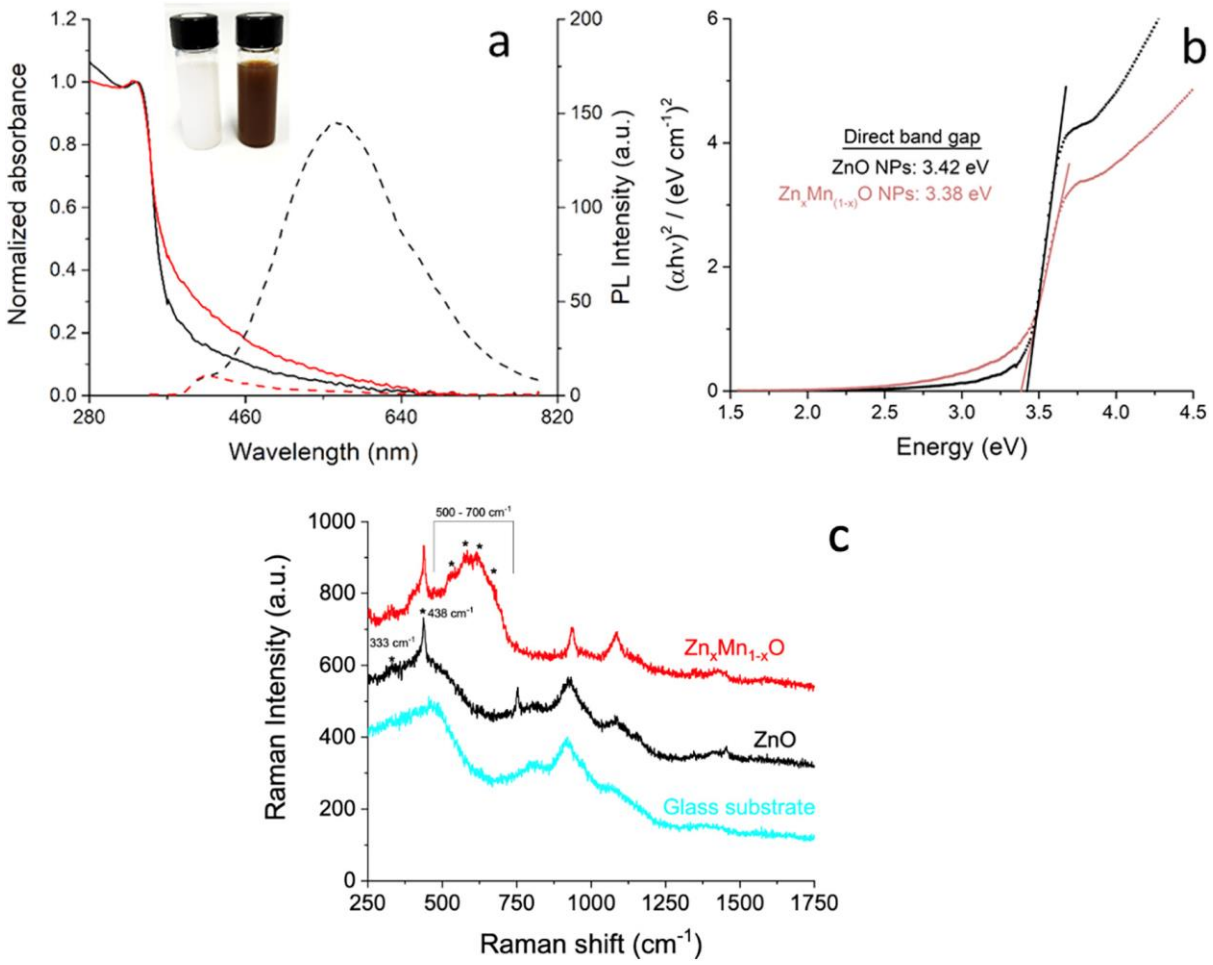

Fig. 2. a) UV/vis absorption (solid lines; left y-axis) and fluorescence emission (dashed lines, right y-axis) spectra of ZnO (black) and $Zn_xMn_{(1-x)}O$ (red) NPs suspensions in DMSO. Inset: photo of 16.3 mg/mL suspensions of ZnO (left) and $Zn_xMn_{(1-x)}O$ (right) NPs. b) Tauc Plot graphs; c) Raman spectra of dried ZnO (black) and $Zn_xMn_{(1-x)}O$ (red) NP deposits on glass; in cyan is reported the reference spectrum of the glass substrate 27 µg/mL concentration, reference DMSO, fluorescence λ_{exc} = 333 nm (abs≃0.2); ii) drop-casting deposition, 200 µL of 16.3 mg/mL suspensions per cm^2, λ_{exc} = 514.5 nm.

The absorption spectrum of $Zn_xMn_{(1-x)}O$ NPs (Fig. 2a, solid red line) displays a profile similar to ZnO suspensions, presenting an edge around 355 nm (3.49 eV) and a peak at around 333 nm

(3.72 eV). Differently from the colourless ZnO suspensions, the spectral region at longer wavelengths presents a more intense absorption, accounting for the brown colour of $Zn_xMn_{(1-x)}O$ NPs. The slight blue shift ($\Delta\lambda = -4$ nm) observed upon comparing the positions of peaks in the absorption profiles of the two NPs suggests that Mn ions might act as well-distributed dopants within the ZnO lattice [[81], [82], [83], [84]]. The band gap value obtained by Tauc plot [77] (Fig. 2b) is 3.38 eV, a value lower than undoped ZnO NPs, in agreement with previous studies [76,85]. Differently from undoped ZnO NPs, no fluorescence emission is observed upon irradiation of the $Zn_xMn_{(1-x)}O$ NPs suspension at the absorption maximum. The action of manganese as a quencher of the emission of ZnO NPs is not unprecedented, and it has been explained in terms of a significant quenching of the electron transitions from surface traps to deep level defects on doping ZnO with Mn ions [86,87].

Fig. 2c presents the Raman spectra of ZnO and $Zn_xMn_{1-x}O$ NPs deposited by drop-casting on a glass substrate. Impurities in the glass cause the presence of fluorescence, which are clearly observable in the spectrum acquired on the substrate (cyan coloured line). These bands strongly affect the ZnO nanoparticles spectrum (black line) However, the narrow and intense peak centred at about 438 cm^{-1}, and assigned to the E_2 (high) mode, emerges by the fluorescence background and characterizes the ZnO NPs spectrum. The typical asymmetric line shape is due to the lattice disorder and to the anharmonic phonon–phonon interactions [88]. Here, it is also possible to distinguish a hint of the second-order vibration mode E_2(high)–E_2(low) centred at about 333 cm^{-1} [89]. In the case of $Zn_xMn_{1-x}O$ NPs sample, the strong absorption of the material in the visible region prevents the excitation radiation from reaching the glass substrate, thus considerably reducing the fluorescence contribution to the Raman spectrum of this sample (red coloured line). As the spectrum lacks the defined peaks typically observed in the presence of stable Mn_3O_4 and

MnO_2 phases, Mn should be present within the ZnO matrix in various oxidation states. Indeed, although the bending mode at about 390 cm^{-1} is hidden by the A_1(TO) and E_1(TO) modes of ZnO vibrating between 370 and 420 cm^{-1} respectively, we clearly observe the Mn O stretching modes lying in the spectral region between 500 and 700 cm^{-1} [90]. In particular, the peak at 528 cm^{-1} can be attributed to a local vibrational mode related to Mn ions compatible with a replacement of Zn ion in the ZnO structure [91], addressing the role of Mn as a dopant. The band at 580 cm^{-1} monitors the presence of the MnO_2 phase; this band is overlapped to other two bands centred at 633 cm^{-1} and 650 cm^{-1}, characteristic of the Mn_2O_3 and Mn_3O_4 species respectively [92]. The higher-frequency peaks in both NPs spectra (red and black lines) can be assigned to the acetate residue signals of the metal precursors.

The morphology of the ZnO and $Zn_xMn_{(1-x)}O$ NPs has been inspected by electronic microscopy. To this end, the NPs are deposited by dip coating onto commercial flat silicon wafers previously cleaned with a UV lamp for 5 min to eliminate any traces of contaminants that can modify the adhesion of the nanomaterials on substrates. Fig. 3 reports the SEM images of ZnO and $Zn_xMn_{(1-x)}O$ NPs, respectively. The low-magnification images (Fig. 3a, b) show continuous film composed of aggregated NPs along the entire surface of the samples. Although aggregation makes precise distribution of their size difficult, an estimation of the diameter of both NPs can be obtained from SEM high-magnification images (Fig. 3c, d) and STEM images (Fig. 3e, f) that can provide a size in the range of 10–20 nm.

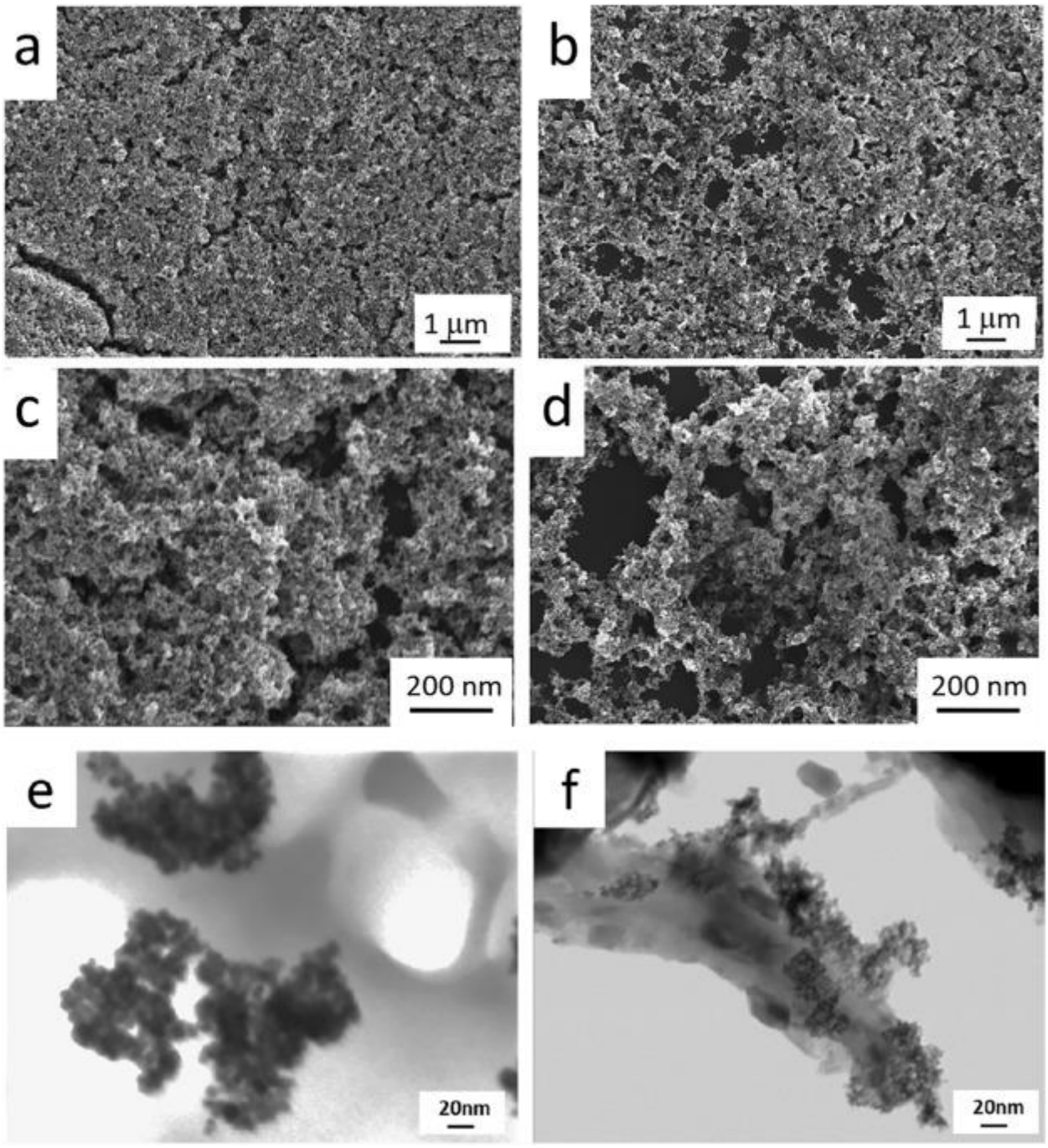

Fig. 3. SEM analysis of ZnO (a, c) and $Zn_xMn_{(1-x)}O$ (b, d) NPs dip coated on flat silicon; STEM of ZnO (e) and $Zn_xMn_{(1-x)}O$ (f) NPs dip coated on flat silicon.

The structural analysis of the ZnO@Ti and $Zn_xMn_{(1-x)}O$@Ti scaffolds has been performed by SEM and Energy Dispersive X-ray (EDX) analysis. Fig. 4a and d shows low- and high-magnification SEM images of uncoated Ti scaffold constituted of a reticular weft with pores of around 0.1 mm^2. At a larger scale, the scaffold surface appears formed by numerous welded spheres as a result of the sintering process during the fabrication of the material. At a higher magnification, the Ti surface is still rough and appears to consist of laterally stacked lamellae [93]. Fig. 4 also reports SEM micrographs of Ti scaffolds after the deposition of ZnO (b, e) and $Zn_xMn_{(1-x)}O$ (c, f) NPs, respectively. The metal surface presents a uniform NPs coverage in both cases, as highlighted by the fractures that feasibly form in the coating upon the evaporation of DMSO following the dip-coating process. The highest magnification images of the coated samples (e, f) at low coverage sites allow roughly estimating the diameter value of the NPs around 20 nm that are in agreement with the colloidal size obtained during the synthesis (see above and Fig. 3).

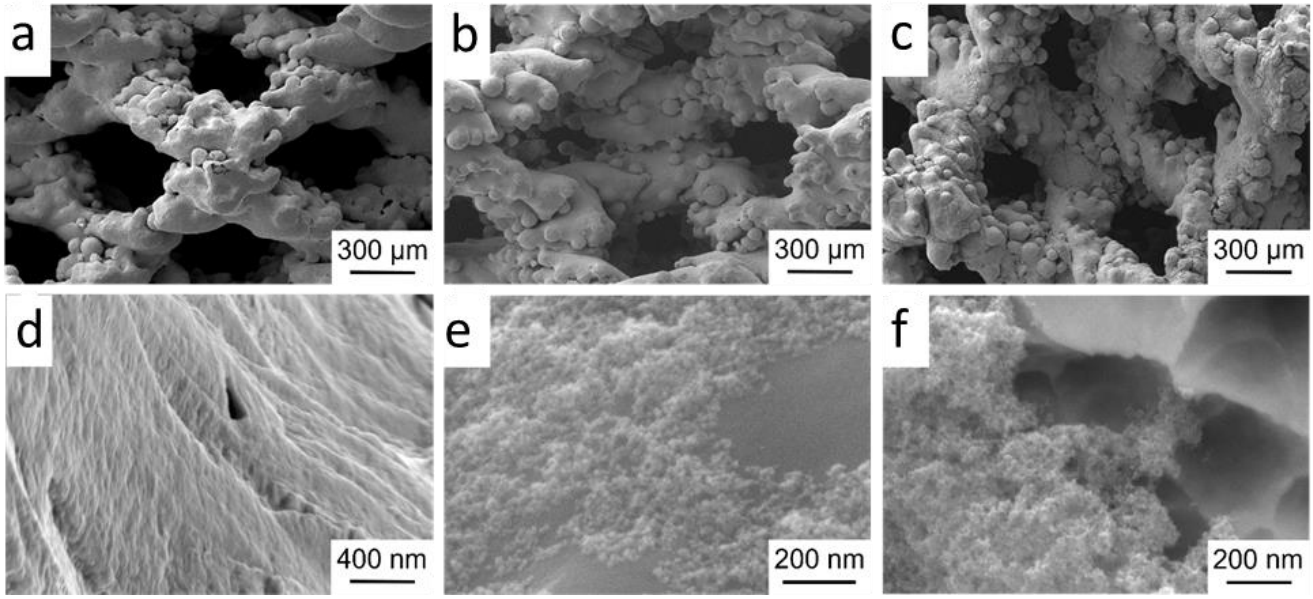

Fig. 4. SEM analysis of ZnO (b, e) and $Zn_xMn_{(1-x)}O$ (c, f) NPs dip coated on Ti scaffolds (a, d). Bare Ti scaffold (a, d) is shown for comparison.

Table 1 reports the EDX analysis results of uncoated Ti and ZnO@Ti, $Zn_xMn_{(1-x)}O$@Ti scaffolds. EDX data collected on uncoated Ti surfaces reflect the composition of a Ti-Al6-V4 alloy conventionally employed in orthopaedic implants, together with a detectable amount of oxygen due to surface oxidation by the cleaning piranha solution. The coating of the Ti surface with ZnO NPs is confirmed on the one hand by the detection of a conspicuous amount of Zn atoms accompanied by the increase in the percentage of oxygen. On the other hand, the surface coverage is indicated by the reduction of the ratio between Ti and O signals. In the case of $Zn_xMn_{(1-x)}O$ NP coatings, this reduction is even more evident, indicating the formation of a nanostructured layer thicker than the ZnO@Ti. Moreover, the amount of Mn in the nanostructured layer is very low, at the limit of detection of the instrument (0.3 %).

Table 1. EDX data for uncoated Ti and ZnO@Ti, $Zn_xMn_{(1-x)}O$ @Ti scaffolds. Detected elements reported as wt% with the relative σ.

Ti Sample	**Ti**		**Al**		**V**		**O**		**Zn**		**Mn**	
	wt%	***σ***	***wt%***	***σ***	***wt%***	***σ***	***wt%***	***σ***	***wt%***	***σ***	***wt%***	***σ***
Uncoated Ti	83.9	2.7	6.7	0.6	1.3	1.9	8.1	2.2	-	-	-	-
ZnO@Ti	52.2	2.1	6.1	0.6	0.4	1.5	15.3	2	25.9	1.5	-	-
$Zn_xMn_{1-x}O$@Ti	15.0	1.5	0.7	0.4	0.0	0.0	21.6	1.5	62.5	2.1	0.3	1.8

The antibacterial assessment firstly involves the evaluation of the bactericidal activity of both ZnO and $Zn_xMn_{(1-x)}O$ NPs against *P. aeruginosa* and *S. aureus* bacteria. Results are shown in Fig. 5. Data obtained after 24 h of incubation show that both ZnO and $Zn_xMn_{(1-x)}O$ NPs exhibit antibacterial activities with respect to the control (bacterial culture without NPs). However, $Zn_xMn_{(1-x)}O$ NPs display higher bacterial inhibition (normalized OD_{540}) against the two bacterial

strains than ZnO NPs (left axis of Fig. 5). The percentage of inhibition (% bacterial inhibition) depends on the NPs amount and for *P. aeruginosa* correspond to: (i) 51.3 % ± 0.27 % at 37.5 μg, 64.6 % ± 0.7 % at 75 μg, 83.9 % ± 0.04 % at 150 μg and 100 % at 300 μg and 600 μg for ZnO NPs; (ii) 59.1 % ± 0.2 % at 37.5 μg, 76.3 % ± 0.2 % at 75 μg, 94.4 % ± 0.1 % at 150 μg and 100 % at 300 μg and 600 μg for $Zn_xMn_{(1-x)}O$ NPs. In case of *S. aureus* these values are: (i) 30.6 % ± 0.09 % at 37.5 μg, 76.4.% ± 0.3 % at 75 μg, 91.7 % ± 0.1 % at 150 μg and 100 % at 300 μg and 600 μg for ZnO NPs; (ii) 77.6 % ± 0.1 % at 37.5 μg, 90.4 % ± 0.1 % at 75 μg, 95.5 % ± 0.03 % at 150 μg and 100 % at 300 μg and 600 μg for $Zn_xMn_{(1-x)}O$ NPs (right axis of Fig. 5).

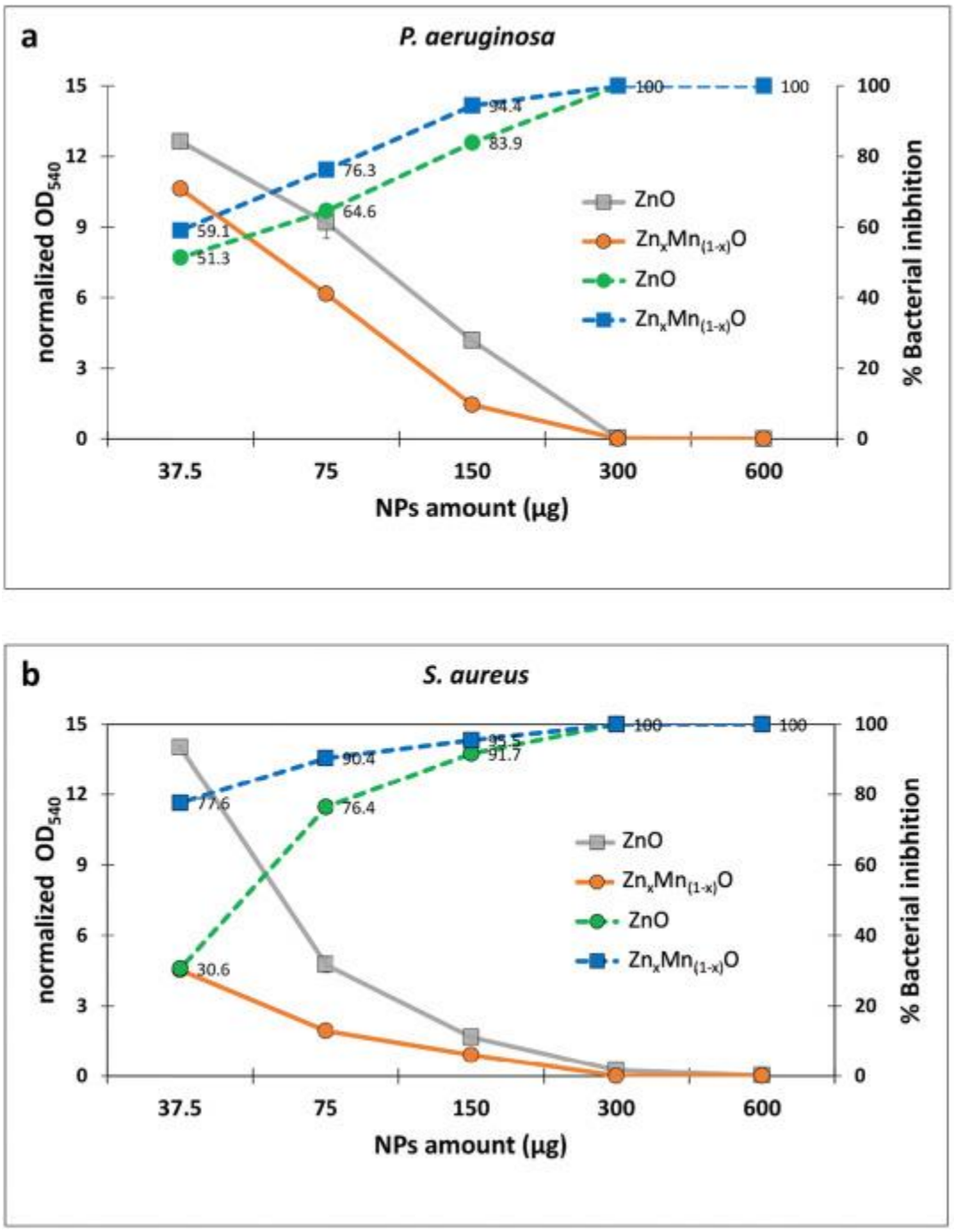

Fig. 5. Bactericidal activity (normalized OD_{540}) (solid lines, left axis) and percentage of bacterial inhibition (dotted lines, right axis) of ZnO NPs and $ZnxMn_{(1-x)}O$ NPs against *P. aeruginosa* (a) and *S. aureus* (b) after 24 h of incubation. CTR+: bacterial culture alone (positive control). MIC = *% bacterial inhibition* > 90 %.

Based on the above-reported data, $Zn_xMn_{(1-x)}O$ NPs show lower MIC values compared to ZnO NPs for both strains, equal to 150 µg ($Zn_xMn_{(1-x)}O$ NPs) vs 300 µg (ZnO NPs) for *P. aeruginosa* and 75 µg ($Zn_xMn_{(1-x)}O$ NPs) vs 150 µg (ZnO NPs) for *S. aureus*.

This behavior can be attributed to a lower band gap of $Zn_xMn_{(1-x)}O$ NPs (3.37 eV) with respect to ZnO NPs (3.42 eV) that triggers an enhanced antibacterial effect primarily through ROS-mediated pathway [81,82].

After the characterization of the NPs in suspension, we focused our study on the bactericidal activity of coated titanium scaffolds with ZnO and $Zn_xMn_{(1-x)}O$ NPs (ZnO@Ti and $Zn_xMn_{(1-x)}O$@Ti). Cell viability on planktonic and adhered bacteria has been evaluated after 24 h of incubation and is shown in Fig. 6.

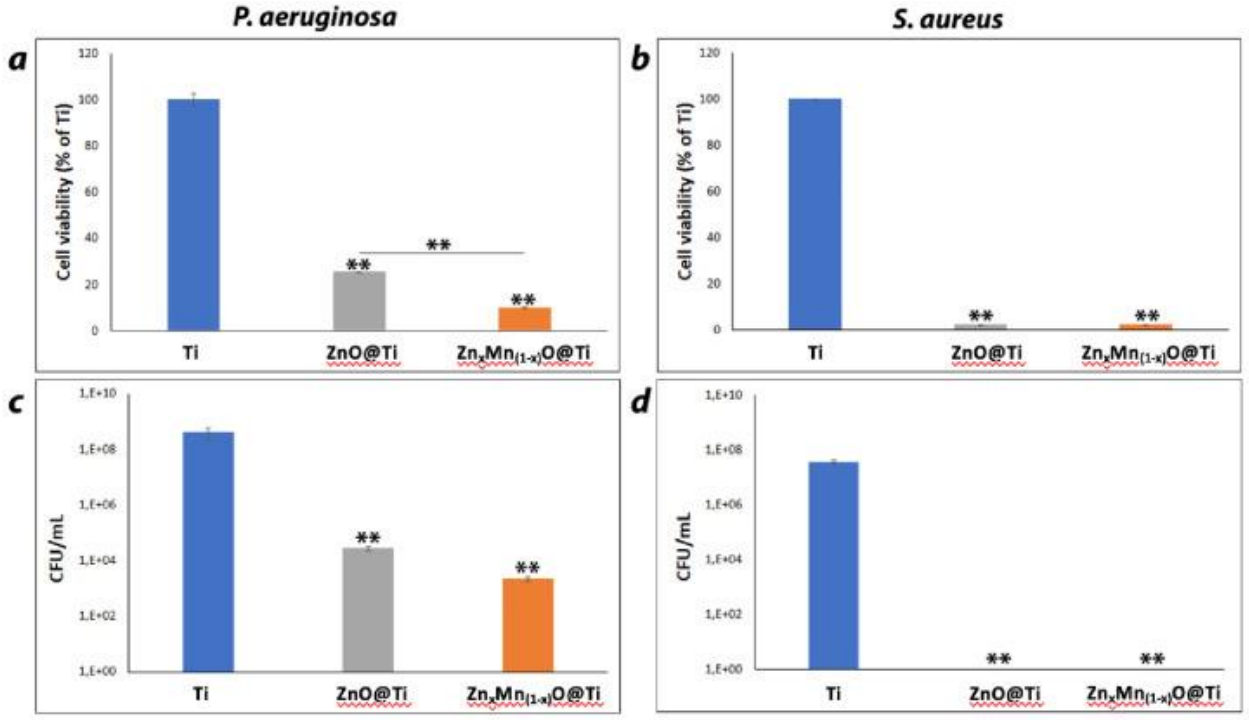

Fig. 6. Antimicrobial activity of Ti uncoated, ZnO@Ti, and $Zn_xMn_{(1-x)}O$@Ti scaffolds against *P. aeruginosa* (a, c) and *S. aureus* (b, d) planktonic and adherent cells after 24 h of incubation. Data are shown

as mean ± standard deviation. **$p < 0.01$ show significant differences between different scaffolds, as reported by the Holm post-hoc test.

Data indicate that both ZnO@Ti and $Zn_xMn_{(1-x)}O$@Ti scaffolds significantly reduced the growth of *P. aeruginosa* and *S. aureus*, compared to the uncoated Ti scaffold (Fig. 6a, b) that do not shows any inhibitory effect on the cell growth of both bacterial strains compared to the control (bacterial culture without NPs) (data not shown). Specifically, after 24 h of incubation, *P. aeruginosa* displays a significant decrease in cell viability of about 74.5 % ± 0.1 % for ZnO@Ti and 89.96 % ± 0.04 % for $Zn_xMn_{(1-x)}O$@Ti compared to the uncoated Ti scaffold. Further, the $Zn_xMn_{(1-x)}O$@Ti scaffold shows a significant (**$p < 0.01$) lower bacterial viability of about 39 % compared to the ZnO@Ti one ($Zn_xMn_{(1-x)}O$@Ti: 10.04 ± 0.04 % vs ZnO@Ti: 25.5 ± 0.1 %). For *S. aureus*, a similar significant cell viability reduction of about 97.70 ± 0.02 % for ZnO@Ti and 97.60 ± 0.01 % for $Zn_xMn_{(1-x)}O$@Ti is observed.

Results on residual adherent cells onto the MO_x@Ti scaffold surfaces (Fig. 6c, d) highlight similar behaviors to those observed in the planktonic cells (Fig. 6a, b). Results indicated that the CFU of adherent *P. aeruginosa* on ZnO@Ti and $Zn_xMn_{(1-x)}O$@Ti scaffolds are $2.6 \pm 0.5 \times 10^4$ and $2.2 \pm 0.4 \times 10^3$, respectively, compared to $3.95 \pm 1.8 \times 10^8$ of uncoated Ti scaffold (Fig. 6c). Notably, $Zn_xMn_{(1-x)}O$@Ti exhibits a decrease of adhered bacteria of five orders of magnitude compared to uncoated Ti (10^3 vs 10^8), while ZnO@Ti shows a reduction of four orders of magnitude (10^4 vs 10^8). With respect to ZnO@Ti scaffolds, the $Zn_xMn_{(1-x)}O$@Ti ones show one order of magnitude of reduction (10^3 vs 10^4). Differently, for *S. aureus* no colonies are observed on both ZnO@Ti and $Zn_xMn_{(1-x)}O$@Ti scaffolds (uncoated Ti scaffold $3.5 \pm 0.7 \times 10^7$ CFU/mL) (Fig. 6d). Basically. *S. aureus* is completely eradicated in presence of coated scaffolds.

These results are in agreement with those above discussed on NP suspensions, confirming that (i) $Zn_xMn_{(1-x)}O$ nanocoating display higher antibacterial activity against the two bacterial strains compared to ZnO NPs derivatization; (ii) Gram-positive bacteria (*S. aureus*) exhibit a higher susceptibility than Gram-negative bacteria (*P. aeruginosa*) for both nanocoatings. Noteworthy, although ZnO@Ti and $Zn_xMn_{(1-x)}O$@Ti scaffolds exhibit similar antibacterial activity to NPs in suspension, this activity is reached with a much lower amount of NPs than the colloidal solution. Actually, the amount of NPs that can be estimated in nanocoatings is below μg, as they can be roughly evaluated by the UV–vis spectra that are unmodified after the dipping process (data not shown). The bacterial reduction exhibited by the nanofunctionalized scaffolds of 90 % for *P. aeruginosa* and 97 % for *S. aureus* corresponds to MIC values for NPs in suspension of 150–300 μg and 75–150 μg, respectively. These amounts are >3 orders of magnitude higher than NPs amount estimated on the coated surface. Based on the above consideration, it appears that the antibacterial activity of both ZnO and $Zn_xMn_{(1-x)}O$ NPs is enhanced when integrated into the Ti scaffold. This improvement can probably be due to the increased availability of NPs that are spread in a continuous nanostructured film onto the trabecular structure of the Ti scaffold, enhancing the probability of surface-bacteria interaction. On the contrary, when NPs are tested in solution, they tend to form aggregates due to the presence of water (see above), which decreases their availability for the interaction of bacteria. Further experiments are ongoing in our lab to better investigate this aspect by assessing the antibacterial activity as a function of the surface-to-volume ratio of the nanofunctionalized scaffolds.

To investigate the antibacterial mechanism, we assess the metal ions release from both ZnO@Ti and $Zn_xMn_{(1-x)}O$@Ti scaffolds according to the procedure reported in [50]. ICP MS experiments showed that at 24 h (the critical time for the antibacterial activity) values of 6.4 μg for Zn^{2+} in

ZnO@Ti scaffold and 6.8 μg for Zn^{2+} and 13 ng for Mn^{2+} in $Zn_xMn_{(1-x)}O$ @Ti scaffold were found. This should indicate that the antibacterial effect is due to the metal ions release. In addition, we also evaluated the release to more long time (72 h) observing an increased release of both Zn^{2+} and Mn^{2+} metal ions up to 8.5 μg for Zn in ZnO@Ti scaffold and 8.3 μg for Zn and 32 ng for $Zn_xMn_{(1-x)}O$ @Ti scaffold. This evidence highlights that the amount of released ions contributes to maintain over time the therapeutic effect.

4. Conclusions

This work presents a simple, rapid, and cheap chemical nanofunctionalization of Ti scaffolds with colloidal ZnO and $Zn_xMn_{(1-x)}O$ NPs, prepared by a sol-gel method, exhibiting antibacterial activity. Characterization studies indicate the formation of ZnO and $Mn_xZn_{1-x}O$ NPs with a size around 20 nm. UV–vis, fluorescence, and Raman spectra suggest that Mn ions act as dopants in the ZnO lattice. Ti scaffolds are functionalized through dip coating and present a continuous film of NPs, producing a nanostructured surface. ZnO@Ti and $Zn_xMn_{(1-x)}O$@Ti display an enhanced antibacterial activity against Gram-positive and Gram-negative bacterial strains compared to NPs in solution. Actually, the bacterial reduction exhibited by the nanofunctionalized scaffolds of 90 % for *P. aeruginosa* and 97 % for *S. aureus* corresponds to MIC values of NPs in suspension of 150–300 μg and 75–150 μg, respectively. These amounts are >3 orders of magnitude higher than NPs amount estimated on the coated surface. Additionally, $Zn_xMn_{(1-x)}O$@Ti shows better performance with respect to ZnO@Ti, reaching a complete eradication for *S. aureus* and a 90 % reduction for *P. aeruginosa*. This eradication can be attributed to both Zn^{2+} and Mn^{2+} metal ions release, as observed by ICP MS experiments that also indicate a therapeutic effect that should be maintained over time (72 h). To the best of our knowledge, it is the first study reported in the literature

describing ZnO and Mn-doped ZnO NPs nanofuctionalized Ti scaffold with improved antibacterial performance, paving the way for the realization of new hybrid implantable devices through a low-cost process, compatible with the biotechnological industrial chain method.

FUNDING

This research was funded by the Italian Ministry of Economics - Project MISE ORTHO Line: *Development of a Production Line for Implantable Medical Devices* - Prog. n. F/190169/01 - 03/X44. The funders had no role in study design, data collection and analysis, decision to publish, or preparation of the manuscript.

CRediT AUTHORSHIP CONTRIBUTION STATEMENT

Giovanna Calabrese: Methodology, Validation. **Giovanna De Luca:** Methodology, Formal analysis. **Domenico Franco:** Investigation, Formal analysis. **Dario Morganti:** Investigation, Data curation. **Maria Giovanna Rizzo:** Investigation. **Anna Bonavita:** Investigation. **Giovanni Neri:** Methodology. **Enza Fazio:** Investigation, Data curation. **Fortunato Neri:** Methodology. **Barbara Fazio:** Investigation, Formal analysis. **Francesco Crea:** Investigation, Data curation. **Antonio Alessio Leonardi:** Investigation. **Maria Josè Lo Faro:** Investigation. **Salvatore Guglielmino:** Methodology. **Sabrina Conoci:** Conceptualization, Methodology, Writing – review & editing.

DECLARATION OF COMPETING INTEREST

The authors declare that they have no known competing financial interests or personal relationships that could have appeared to influence the work reported in this paper.

ACKNOWLEDGMENT

Authors thank Prof. Francesco Nastasi and Prof. Fausto Puntoriero for their support in fluorescence spectra recording and Antonina De Francesco for experimental support.

DATA AVAILABILITY

Data will be made available on request.

REFERENCES

[1] C. Ringot, V. Sol, M. Barrière, N. Saad, P. Bressollier, R. Granet, P. Couleaud, C. Frochot, K.P. Triazinyl. Porphyrin-based photoactive cotton fabrics: preparation, characterization, and antibacterial activity. Biomacromolecules, 12 (2011), pp. 1716-1723, 10.1021/bm200082d

[2] El-R. Kenawy, S.D. Worley, R. Broughton. The chemistry and applications of antimicrobial polymers: a state-of-the-art review. Biomacromolecules, 8 (5) (2007), pp. 1359-1384, 10.1021/bm061150q

[3] M. Jayandran, M. Haneefa, V. Balasubramanian. Green synthesis and characterization of manganese nanoparticles using natural plant extracts and its evaluation of antimicrobial activity. J. Appl. Pharm. Sci., 5 (2015), pp. 105-110, 10.7324/JAPS.2015.501218

[4] U. Kamran, H.N. Bhatti, M. Iqbal, S. Jamil, M. Zahid. Biogenic synthesis, characterization and investigation of photocatalytic and antimicrobial activity of manganese nanoparticles synthesized from Cinnamomum verum bark extract. J. Mol. Struct., 1179 (2019), pp. 532-539, 10.1016/j.molstruc.2018.11.006

[5] E. Azhir, R. Etefagh, N. Shahtahmasebi, M. Mashreghi, P. Pordeli. Preparation, characterization and antibacterial activity of manganese oxide nanoparticles. Phys. Chem. Res., 3 (2015), pp. 197-204, 10.22036/pcr.2015.9329

[6] L. Montanaro, D. Campoccia, C.R. Arciola. Advancements in molecular epidemiology of implant infections and future perspectives. Biomaterials, 28 (2007), pp. 5155-5168, 10.1016/j.biomaterials.2007.08.003

[7] C.R. Arciola, L. Visai, F. Testoni, S. Arciola, D. Campoccia, P. Speziale, L. Montanaro. Concise survey of staphylococcus aureus virulence factors that promote adhesion and damage to peri-implant tissues. Int. J. Artif. Org., 34 (2011), pp. 771-780, 10.5301/ijao.5000046

[8] L. Montanaro, F. Testoni, A. Poggi, L. Visai, P. Speziale, C.R. Arciola. Emerging pathogenetic mechanisms of the implant-related osteomyelitis by Staphylococcus aureus. Int. J. Artif. Org., 34 (2011), pp. 781-788, 10.5301/ijao.5000052

[9] D. Campoccia, L. Montanaro, C.R. Arciola. The significance of infection related to orthopedic devices and issues of antibiotic resistance. Biomaterials, 27 (2006), pp. 2331-2339, 10.1016/j.biomaterials.2005.11.044

[10] S.X. Liang, X.J. Feng, L.X. Yin, X.Y. Liu, M.Z. Ma, R.P. Liu. Development of a new β Ti alloy with low modulus and favorable plasticity for implant material. Mater. Sci. Eng. C, 61 (2016), pp. 338-343, 10.1016/j.msec.2015.12.076

[11] M. Long, H.J. Rack. Titanium alloys in total joint replacement - a materials science perspective. Biomaterials, 19 (1998), pp. 1621-1639, 10.1016/S0142-9612(97)00146-4

[12] S. Attarilar, M.T. Salehi, K.J. Al-Fadhalah, F. Djavanroodi, M. Mozafari. Functionally graded titanium implants: characteristic enhancement induced by combined severe plastic deformation. PLoS One, 14 (2019), Article e0221491, 10.1371/journal.pone.0221491

[13] W. Zhu, S. Shao, L. Xu, W. Chen, X. Yu, K. Tang, Z. Tang, F. Zhang, J. Qiu. Enhanced corrosion resistance of zinc-containing nanowires-modified titanium surface under exposure to oxidizing microenvironment. J. Nanobiotechnol., 17 (2019), p. 55, 10.1186/s12951-019-0488-9

[14] R. Malhotra, Y.M. Han, J.L.P. Morin, E.K. Kuong-Van, R.J.J. Chew, A.H. Castro Neto, C.A. Nijhuis, V. Rosa. Inhibiting corrosion of biomedical-grade Ti-6Al-4V alloys with graphene nanocoating. J. Dent. Res., 99 (2020), pp. 285-292, 10.1177/0022034519897003

[15] T. Lei, W. Zhang, H. Qian, P.N. Lim, E.S. Thian, P. Lei, Y. Hu, Z. Wang

Silicon-incorporated nanohydroxyapatite-reinforced poly(ε-caprolactone) film to enhance osteogenesis for bone tissue engineering applications. Colloids Surf. B: Biointerfaces, 187 (2020), p. 110714, 10.1016/j.colsurfb.2019.110714

[16] C. Zhu, Y. Lv, C. Qian, H. Qian, T. Jiao, L. Wang, F. Zhang. Proliferation and osteogenic differentiation of rat BMSCs on a novel Ti/SiC metal matrix nanocomposite modified by friction stir processing. Sci. Rep., 6 (2016), p. 38875, 10.1038/srep38875

[17] C. Wagner, G.M. Hänsch. Mechanisms of bacterial colonization of implants and host response. Adv. Exp. Med. Biol., 971 (2017), pp. 15-27, 10.1007/5584_2016_173

[18] J. Josse, F. Valour, Y. Maali, A. Diot, C. Batailler, T. Ferry, F. Laurent. Interaction between staphylococcal biofilm and bone: how does the presence of biofilm promote prosthesis loosening? Front. Microbiol., 10 (2019), p. 1602, 10.3389/fmicb.2019.01602

[19] C.R. Arciola, D. Campoccia, L. Montanaro. Implant infections: adhesion, biofilm formation and immune evasion. Nat. Rev. Microbiol., 16 (2018), pp. 397-409, 10.1038/s41579-018-0019-y

[20] L. Thomer, O. Schneewind, D. Missiakas. Pathogenesis of Staphylococcus aureus bloodstream infections. Annu. Rev. Pathol., 11 (2016), pp. 343-364, 10.1146/annurev-pathol-012615-044351

[21] S. Steinmetz, D. Wernly, K. Moerenhout, A. Trampuz, O. Borens. Infection after fracture fixation. EFORT Open Rev., 4 (2019), pp. 468-475, 10.1302/2058-5241.4.180093

[22] M.A. Burch, T.F. Moriarty, R. Kuehl, A. Foster, M. Morgenstern. Complications in orthopedic trauma surgery: fracture-related infection. B. Li, T.F. Moriarty, T. Webster, M. Xing (Eds.), Racing for the Surface: Pathogenesis of Implant Infection and Advanced Antimicrobial

Strategies, Springer International Publishing, Cham (2020), pp. 33-56, 10.1007/978-3-030-34475-7_2

[23] Z. Jones, A.E. Brooks, Z. Ferrell, D.W. Grainger, K.D. Sinclair. A resorbable antibiotic eluting bone void filler for periprosthetic joint infection prevention. J Biomed Mater Res B Appl Biomater, 104 (2016), pp. 1632-1642, 10.1002/jbm.b.33513

[24] P.R. Oliveira, V.C. Carvalho, A.L.M. Lima. Optimizing the treatment of osteomyelitis with antimicrobial drugs: current concepts. Curr. Orthop. Pract., 28 (2017), pp. 208-212, 10.1097/BCO.0000000000000477

[25] B. Li, T.J. Webster. Bacteria antibiotic resistance: new challenges and opportunities for implant-associated orthopedic infections. J. Orthop. Res., 36 (2018), pp. 22-32, 10.1002/jor.23656

[26] R. Roy, M. Tiwari, G. Donelli, V. Tiwari. Strategies for combating bacterial biofilms: a focus on anti-biofilm agents and their mechanisms of action. Virulence, 9 (2017), pp. 522-554, 10.1080/21505594.2017.1313372

[27] G. Calabrese, S. Petralia, C. Fabbi, S. Forte, D. Franco, S. Guglielmino, E. Esposito, S. Cuzzocrea, F. Traina, S. Conoci. Au, Pd and maghemite nanofunctionalized hydroxyapatite scaffolds for bone regeneration. Regen. Biomater., 7 (2020), pp. 461-469, 10.1093/rb/rbaa033

[28] H. Chouirfa, H. Bouloussa, V. Migonney, C. Falentin-Daudré. Review of titanium surface modification techniques and coatings for antibacterial applications. Acta Biomater., 83 (2019), pp. 37-54, 10.1016/j.actbio.2018.10.036

[29] J. Liu, S. Attarilar, C. Wang, M. Tamaddon, C. Yang, K. Xie, J. Yao, L. Wang, C. Liu, Y. Tang. Nano-modified titanium implant materials: a way toward improved antibacterial properties. Front. Bioeng. Biotechnol., 8 (2020), p. 576969, 10.3389/fbioe.2020.576969

[30] G. Calabrese, D. Franco, S. Petralia, F. Monforte, G.G. Condorelli, S. Squarzoni, F. Traina, S. Conoci. Dual-functional nano-functionalized titanium scaffolds to inhibit bacterial growth and enhance osteointegration. Nanomaterials, 11 (2021), p. 2634, 10.3390/nano11102634

[31] D. Franco, G. Calabrese, S. Petralia, G. Neri, C. Corsaro, L. Forte, S. Squarzoni, S. Guglielmino, F. Traina, E. Fazio, S. Conoci. Antimicrobial effect and cytotoxic evaluation of Mg-doped hydroxyapatite functionalized with Au-nano rods. Molecules, 26 (2021), p. 1099, 10.3390/molecules26041099

[32] G. Nocito, E.L. Sciuto, D. Franco, F. Nastasi, L. Pulvirenti, S. Petralia, C. Spinella, G. Calabrese, S. Guglielmino, S. Conoci. Physicochemical characterization and antibacterial properties of carbon dots from two Mediterranean olive solid waste cultivars. Nanomaterials, 12 (2022), p. 885, 10.3390/nano12050885

[33] I. Sondi, B. Salopek-Sondi. Silver nanoparticles as antimicrobial agent: a case study on E. coli as a model for gram-negative bacteria. J. Colloid Interface Sci., 275 (2004), pp. 177-182, 10.1016/j.jcis.2004.02.012

[34] W.R. Li, X.-B. Xie, Q.-S. Shi, H.-Y. Zeng, Y.-S. OU-Yang, Y.-B. Chen. Antibacterial activity and mechanism of silver nanoparticles on Escherichia coli. Appl. Microbiol. Biotechnol., 85 (2010), pp. 1115-1122, 10.1007/s00253-009-2159-5

[35] G. Calabrese, S. Petralia, D. Franco, G. Nocito, C. Fabbi, L. Forte, S. Guglielmino, S. Squarzoni, F. Traina, S. Conoci. A new Ag-nanostructured hydroxyapatite porous scaffold: antibacterial effect and cytotoxicity study. Mater. Sci. Eng. C, 118 (2021), p. 111394, 10.1016/j.msec.2020.111394

[36] C. Liao, Y. Li, S.C. Tjong. Bactericidal and cytotoxic properties of silver nanoparticles. Int. J. Mol. Sci., 20 (2019), p. 449, 10.3390/ijms20020449

[37] S. Kittler, C. Greulich, J. Diendorf, M. Köller, M. Epple. Toxicity of silver nanoparticles increases during storage because of slow dissolution under release of silver ions. Chem. Mater., 22 (2010), pp. 4548-4554, 10.1021/cm100023p

[38] J. Pasquet, Y. Chevalier, E. Couval, D. Bouvier, G. Noizet, C. Morlière, M.A. Bolzinger. Antimicrobial activity of zinc oxide particles on five micro-organisms of the challenge tests related to their physicochemical properties. Int. J. Pharm., 460 (2014), pp. 92-100, 10.1016/j.ijpharm.2013.10.031

[39] T.J. Wood, A. Hurst, E. Schofield, L. Thompson, G. Oswald, O. Evans, J. Sharples, C. Pearson, C. Petty, S. Badyal. Electroless deposition of multi-functional zinc oxide surfaces displaying photoconductive, superhydrophobic, photowetting, and antibacterial properties. J. Mater. Chem., 22 (2012), pp. 3859-3867, 10.1039/C2JM14260K

[40] E. Malka, I. Perelshtein, A. Lipovsky, Y. Shalom, L. Naparstek, N. Perkas, T. Patick, R. Lubart, Y. Nitzan, E. Banin, A. Gedanken. Eradication of multi-drug resistant bacteria by a novel Zn-doped CuO nanocomposite. Small, 9 (2013), pp. 4069-4076, 10.1002/smll.201301081

[41] A.R. Deokar, Y. Shalom, I. Perelshtein, N. Perkas, A. Gedanken, E. Banin. A topical antibacterial ointment made of Zn-doped copper oxide nanocomposite. J. Nanopart. Res., 18 (2016), p. 218, 10.1007/s11051-016-3534-7

[42] M. Urso, S.G. Leonardi, G. Neri, S. Petralia, S. Conoci, F. Priolo, S. Mirabella. Room temperature detection and modelling of sub-ppm NO2 by low-cost nanoporous NiO film. Sensors Actuators B Chem., 305 (2020), p. 12748, 10.1016/j.snb.2019.127481

[43] R. Manjula, M. Thenmozhi, S. Thilagavathi, R. Srinivasan, A. Kathirvel. Green synthesis and characterization of manganese oxide nanoparticles from Gardenia resinifera leaves. Mater. Today Proc., 26 (2020), pp. 3559-3563, 10.1016/j.matpr.2019.07.396

[44] A. Król, P. Pomastowski, K. Rafińska, V. Railean-Plugaru, B. Buszewski. Zinc oxide nanoparticles: synthesis, antiseptic activity and toxicity mechanism. Adv. Colloid Interf. Sci., 249 (2017), pp. 37-52, 10.1016/j.cis.2017.07.033

[45] A. Ali, A.R. Phull, M. Zia. Elemental zinc to zinc nanoparticles: is ZnO NPs crucial for life? Synthesis, toxicological, and environmental concerns. Nanotechnol. Rev., 7 (2018), pp. 413-441, 10.1515/ntrev-2018-0067

[46] S.J. Choi, J.H. Choy. Biokinetics of zinc oxide nanoparticles: toxicokinetics, biological fates, and protein interaction. Int. J. Nanomedicine, 9 (2014), pp. 261-269, 10.2147/IJN.S57920

[47] K. Ravichandran, K. Karthika, B. Sakthivel, N. Jabena Begum, S. Snega, K. Swaminathan, V. Senthamilselvi. Tuning the combined magnetic and antibacterial properties of ZnO

nanopowders through Mn doping for biomedical applications. J. Magn. Magn. Mater., 358–359 (2014), pp. 50-55, 10.1016/j.jmmm.2014.01.008

[48] J. Iqbal, N. Safdar, T. Jan, M. Ismail, S.S. Hussain, A. Mahmood, S. Shahzad, Q. Mansoor. Facile synthesis as well as structural, Raman, dielectric and antibacterial characteristics of Cu doped ZnO nanoparticles. J. Mater. Sci. Technol., 31 (2015), pp. 300-304, 10.1016/j.jmst.2014.06.013

[49] N. Padmavathy, R. Vijayaraghavan. Enhanced bioactivity of ZnO nanoparticles - an antimicrobial study. Sci. Technol. Adv. Mater., 9 (2008), Article 035004, 10.1088/1468-6996/9/3/035004

[50] L. Grenho, C.L. Salgado, M.H. Fernandes, F.J. Monteiro, M.P. Ferraz. Antibacterial activity and biocompatibility of three-dimensional nanostructured porous granules of hydroxyapatite and zinc oxide nanoparticles. Nanotechnology, 26 (2015), p. 315101, 10.1088/0957-4484/26/31/315101

[51] R. Augustine, H.N. Malik, D.K. Singhal, A. Mukherjee, D. Malakar, N. Kalarikkal, S. Thomas. Electrospun polycaprolactone/ZnO nanocomposite membranes as biomaterials with antibacterial and cell adhesion properties. J. Polym. Res., 21 (2014), p. 347, 10.1007/s10965-013-0347-6

[52] S.V. Gudkov, D.E. Burmistrov, D.A. Serov, M.B. Rebezov, A.A. Semenova, A.B. Lisitsyn. A mini review of antibacterial properties of ZnO nanoparticles. Front. Phys., 9 (2021), Article 641481, 10.3389/fphy.2021.641481

[53] R.Y. Pelgrift, A.J. Friedman. Nanotechnology as a therapeutic tool to combat microbial resistance. Adv. Drug Deliv. Rev., 65 (2013), pp. 1803-1815, 10.1016/j.addr.2013.07.011

[54] M. Laurenti, V. Cauda. ZnO nanostructures for tissue engineering applications. Nanomaterials, 7 (2017), p. 374, 10.3390/nano7110374

[55] L. Cui, J. Liang, H. Liu, K. Zhang, J. Li. Nanomaterials for angiogenesis in skin tissue engineering. Tissue Eng. Part B Rev., 26 (2020), pp. 203-216, 10.1089/ten.teb.2019.0337

[56] M.A. Qamar, M. Javed, S. Shahid. Designing and investigation of enhanced photocatalytic and antibacterial properties of 3d (Fe, Co, Ni, Mn and Cr) metal-doped zinc oxide nanoparticles. Opt. Mater., 126 (2022), p. 112211, 10.1016/j.optmat.2022.112211

[57] P.A. Sukkurji, Y. Fujiwara, N.J. Vasa, M.S.R. Rao, M. Higashihata, D. Nakamura. Optical and magnetic characterization of transition metal ion doped ZnO microspheres synthesized via laser ablation in air. Proceedings of the Laser Resonators, Microresonators, and Beam Control XIX, vol. 10090, SPIE (2017), pp. 234-243, 10.1117/12.2253560

[58] N. Wu, X. Liu, C. Zhao, C. Cui, A. Xia. Effects of particle size on the magnetic and microwave absorption properties of carbon-coated nickel nanocapsules. J. Alloys Compd., 656 (2016), pp. 628-634, 10.1016/j.jallcom.2015.10.027

[59] L. Duan, X. Zhao, J. Liu, W. Geng, H. Xie, S. Chen. Structural, thermal and magnetic investigations of heavily Mn-doped ZnO nanoparticles. J. Magn. Magn. Mater., 323 (2011), pp. 2374-2379, 10.1016/j.jmmm.2011.04.018

[60] R. Dom, L.R. Baby, H.G. Kim, P.H. Borse. Fe controlled charge-dynamics in ZnO for solar hydrogen generation. Int. J. Hydrog. Energy, 42 (2017), pp. 5758-5767, 10.1016/j.ijhydene.2016.12.089

[61] M. Wang, C. Huang, Z. Huang, W. Guo, J. Huang, H. He, H. Wang, Y. Cao, Q. Liu, J. Liang. Synthesis and photoluminescence of Eu-doped ZnO microrods prepared by hydrothermal method. Opt. Mater., 31 (2009), pp. 1502-1505, 10.1016/j.optmat.2009.02.009

[62] S.B. Khan, M.I. Khan, J. Nisar. Microwave assisted green synthesis of pure and Mn-doped ZnO nanocomposites: in vitro anti-bacterial assay and photodegradation of methylene blue. Front. Mater., 8 (2022), p. 491, 10.3389/fmats.2021.710155

[63] Y.M. Hao, S.Y. Lou, S.M. Zhou, R.J. Yuan, G.Y. Zhu, N. Li. Structural, optical, and magnetic studies of manganese-doped zinc oxide hierarchical microspheres by self-assembly of nanoparticles. Nanoscale Res. Lett., 7 (2012), p. 100, 10.1186/1556-276X-7-100

[64] A. Dhanalakshmi, B. Natarajan, V. Ramadas, A. Palanimurugan, S. Thanikaikarasan. Structural, morphological, optical and antibacterial activity of rod-shaped zinc oxide and

manganese-doped zinc oxide nanoparticles. Pramana J. Phys., 87 (2016), p. 57, 10.1007/s12043-016-1248-0

[65] N.S. Norberg, K.R. Kittilstved, J.E. Amonette, R.K. Kukkadapu, D.A. Schwartz, D.R. Gamelin. Synthesis of colloidal Mn2+:ZnO quantum dots and high-TC ferromagnetic nanocrystalline thin films. J. Am. Chem. Soc., 126 (2004), pp. 9387-9398, 10.1021/ja048427j

[66] K. Radhi, L. Devi, B. Chandrasekar, K. Kasirajan, M. Karunakaran, M. Divya Gnaneswari, S. Usha. Enhanced in vitro antibacterial activity of ZnO and Mn–Mg Co-doped ZnO nanoparticles: investigation of synthesis, characterization, and impact of dopant. Appl. Phys. A Mater. Sci. Process., 128 (2022), p. 368, 10.1007/s00339-022-05502-3

[67] Y. Lv, X. Song, T. Lei, P. Yin. Structural and antibacterial properties of doped zinc oxide and their composites with hydroxyapatite. Colloids Surf. A Physicochem. Eng. Asp., 651 (2022), p. 129706, 10.1016/j.colsurfa.2022.129706

[68] L.H. Madkour. Reactive Oxygen Species (ROS), Nanoparticles, and Endoplasmic Reticulum (ER) Stress-induced Cell Death Mechanisms. Academic Press (2020)

[69] B.J. Alloway. Heavy metals and metalloids as micronutrients for plants and animals. B.J. Alloway (Ed.), Heavy Metals in Soils: Trace Metals and Metalloids in Soils and Their Bioavailability, Environmental Pollution, Springer Netherlands, Dordrecht (2013), pp. 195-209, 10.1007/978-94-007-4470-7_7

[70] L. Li, X. Yang. The essential element manganese, oxidative stress, and metabolic diseases: links and interactions. Oxidative Med. Cell. Longev. (2018), Article e7580707, 10.1155/2018/7580707

[71] D. Klimis-Zacas. Manganese in Health and Disease. CRC Press (1993)

[72] S.K. Ghosh. Diversity in the family of manganese oxides at the nanoscale: from fundamentals to applications. ACS Omega, 5 (2020), pp. 25493-25504, 10.1021/acsomega.0c03455

[73] Z. Huang, X. Zheng, D. Yan, G. Yin, X. Liao, Y. Kang, Y. Yao, D. Huang, B. Hao. Toxicological effect of ZnO nanoparticles based on bacteria. Langmuir, 24 (2008), pp. 4140-4144, 10.1021/la7035949

[74] N. Jones, B. Ray, K.T. Ranjit, A.C. Manna. Antibacterial activity of ZnO nanoparticle suspensions on a broad spectrum of microorganisms. FEMS Microbiol. Lett., 279 (2008), pp. 71-76, 10.1111/j.1574-6968.2007.01012.x

[75] Y.H. Leung, C.M.N. Chan, A.M.C. Ng, H.T. Chan, M.W.L. Chiang, A.B. Djurišić, Y.H. Ng, W.Y. Jim, M.Y. Guo, F.C.C. Leung, W.K. Chan, D.T.W. Au. Antibacterial activity of ZnO nanoparticles with a modified surface under ambient illumination. Nanotechnology, 23 (2012), Article 475703, 10.1088/0957-4484/23/47/475703

[76] Y.V. Panasiuk, O.E. Raevskaya, O.L. Stroyuk, S.Y. Kuchmiy, V.M. Dzhagan, M. Hietschold, D.R.T. Zahn. Colloidal ZnO nanocrystals in dimethylsulfoxide: a new synthesis, optical, photo- and electroluminescent properties. Nanotechnology, 25 (2014), Article 075601, 10.1088/0957-4484/25/7/075601

[77] J. Tauc. Optical properties and electronic structure of amorphous Ge and Si. Mater. Res. Bull., 3 (1968), pp. 37-46, 10.1016/0025-5408(68)90023-8

[78] P.V. Kamat, B. Patrick. Photophysics and photochemistry of quantized zinc oxide colloids. J. Phys. Chem., 96 (1992), pp. 6829-6834, 10.1021/j100195a055.

[79] A. van Dijken, E.A. Meulenkamp, D. Vanmaekelbergh, A. Meijerink. The kinetics of the radiative and nonradiative processes in nanocrystalline ZnO particles upon photoexcitation. J. Phys. Chem. B, 104 (2000), pp. 1715-1723, 10.1021/jp993327z

[80] Ü. Özgür, Ya.I. Alivov, C. Liu, A. Teke, M.A. Reshchikov, S. Doğan, V. Avrutin, S.J. Cho, H. Morkoç. A comprehensive review of ZnO materials and devices. J. Appl. Phys., 98 (2005), Article 041301, 10.1063/1.1992666

[81] N.R. Yogamalar, A. Chandra Bose. Burstein–Moss shift and room temperature near-band-edge luminescence in lithium-doped zinc oxide. Appl. Phys. A Mater. Sci. Process., 103 (2011), pp. 33-42, 10.1007/s00339-011-6304-5

[82] S. Karamat, S. Mahmood, J.J. Lin, Z.Y. Pan, P. Lee, T.L. Tan, S.V. Springham, R.V. Ramanujan, R.S. Rawat. Structural, optical and magnetic properties of (ZnO)1−x(MnO2)x thin films deposited at room temperature. Appl. Surf. Sci., 254 (2008), pp. 7285-7289, 10.1016/j.apsusc.2008.05.318

[83] N.S. Sabri, A.K. Yahya, M.K. Talari. Emission properties of Mn doped ZnO nanoparticles prepared by mechanochemical processing. J. Lumin., 132 (2012), pp. 1735-1739, 10.1016/j.jlumin.2012.02.020

[84] K.G. Saw, N.M. Aznan, F.K. Yam, S.S. Ng, S.Y. Pung. New insights on the Burstein-Moss shift and band gap narrowing in indium-doped zinc oxide thin films. PLoS One, 10 (2015), Article e0141180, 10.1371/journal.pone.0141180

[85] S.B. Khan, M.I. Khan, J. Nisar. Microwave assisted green synthesis of pure and Mn-DOPED ZnO nanocomposites: in vitro anti-bacterial assay and photodegradation of methylene blue. Front. Mater., 8 (2022), p. 491, 10.3389/fmats.2021.710155

[86] Y.S. Wang, P.J. Thomas, P. O'Brien. Optical properties of ZnO nanocrystals doped with Cd, Mg, Mn, and Fe ions. J. Phys. Chem. B, 110 (2006), pp. 21412-21415, 10.1021/jp0654415

[87] A.G. Ali, F.B. Dejene, H.C. Swart. Effect of Mn doping on the structural and optical properties of sol-gel derived ZnO nanoparticles. Cent. Eur. J. Phys., 10 (2012), pp. 478-484, 10.2478/s11534-011-0106-4

[88] R. Cuscó, E. Alarcón-Lladó, J. Ibáñez, L. Artús, J. Jiménez, B. Wang, J. Michael Callahan. Temperature dependence of Raman scattering in ZnO. Phys. Rev. B Condens. Matter, 75 (2007), Article 165202, 10.1103/PhysRevB.75.165202

[89] Y. Song, S. Zhang, C. Zhang, Y. Yang, K. Lv. Raman spectra and microstructure of zinc oxide irradiated with swift heavy ion. Crystals, 9 (2019), p. 395, 10.3390/cryst9080395

[90] B. Fazio, L. Spadaro, G. Trunfio, J. Negro, F. Arena. Raman scattering of MnOx-CeOx composite catalysts: structural aspects and laser-heating effects. J. Raman Spectrosc., 42 (2011), pp. 1583-1588, 10.1002/jrs.2897

[91] S. Guo, Z. Du, S. Dai. Analysis of Raman modes in Mn-doped ZnO nanocrystals. Phys. Status Solidi B, 246 (2009), pp. 2329-2332, 10.1002/pssb.200945192

[92] F. Arena, G. Trunfio, B. Fazio, J. Negro, L. Spadaro. Nanosize effects, physicochemical properties, and catalytic oxidation pattern of the redox-precipitated MnCeOx system. J. Phys. Chem. C, 113 (7) (2009), pp. 2822-2829, 10.1021/jp8068249

[93] J.C. Russ, F.B. Neal. The Image Processing Handbook. (7th ed.), CRC Press, Boca Raton (2017), 10.1201/b18983